https://doi.org/10.5194/egusphere-2026-6745
Preprint. Discussion started: 17 November 2026
© Author(s) 2026. CC BY 4.0 License.

# Large spatial heterogeneity in historical atmospheric sulfate trends over the Tibetan Plateau inferred from ice-core records

Hongcheng Lu[1], Peng Wang[1], Dandan Yang[2], Tandong Yao[2], Guangjian Wu[2], Huabiao Zhao[2], Xiangying Li[3], and Lei Geng[1, 4, 5]

Correspondence: Lei Geng (genglei@ustc.edu.cn)

[1]National Key Laboratory of Deep Space Exploration/School of Earth and Space Sciences, University of Science and Technology of China, Hefei, China

[2]State Key Laboratory of Tibetan Plateau Earth System, Environment and Resources (TPESER), Institute of Tibetan Plateau Research, Chinese Academy of Sciences, Beijing, China

[3]Shaanxi Key Laboratory of Earth Surface System and Environmental Carrying Capacity, Northwest University, Xi'an, China

[4]Deep Space Exploration Laboratory, Hefei, China

[5]CAS Center for Excellence in Comparative Planetology, University of Science and Technology of China, Hefei, China

**Abstract:** Atmospheric sulfate ($SO_4^{2-}$) influences radiation and cloud processes, yet its multidecadal evolution over the Tibetan Plateau (TP) remains poorly constrained because glacier archives integrate atmospheric supply, deposition, and preservation. We synthesized $SO_4^{2-}$ records from 13 high-elevation ice cores in six regions and compared their concentrations and precipitation-scaled flux proxies with $SO_4^{2-}$ aerosol mass mixing ratios and wet plus dry deposition from 11 models participating in the Coupled Model Intercomparison Project Phase 6 (CMIP6). Mean concentrations are generally higher in the northern and western TP than in southern monsoon-influenced regions, whereas increases since the mid-twentieth century are concentrated mainly along the Plateau margins. Several interior clusters are stable or declining, and paired $SO_4^{2-}$-$Ca^{2+}$ records show site-dependent covariation consistent with spatially variable dust-related influence. CMIP6 models reproduce increases in some marginal regions but simulate a more spatially coherent rise in atmospheric $SO_4^{2-}$ and deposition, including in interior regions with weak or negative ice-core changes. In CESM2-WACCM, which we analyze in detail, atmospheric $SO_4^{2-}$ increases in all six regions at rates several times the largest ice-core rate. The models and the ice cores therefore differ in the sign and spatial pattern of long-term change as well as in its magnitude. These records provide a regional benchmark for evaluating $SO_4^{2-}$ cycling and deposition over the Third Pole.

## 1 Introduction

https://doi.org/10.5194/egusphere-2026-6745
Preprint. Discussion started: 17 November 2026
© Author(s) 2026. CC BY 4.0 License.

Atmospheric $SO_4^{2-}$ scatters solar radiation and modifies cloud properties (Twomey, 1977; Carslaw et al., 2013). Its abundance reflects sulfur emissions, oxidation chemistry, atmospheric transport, cloud processing, and wet and dry removal. Over the Tibetan Plateau (TP), these processes interact with steep terrain, monsoon and westerly circulation, uneven precipitation, and abundant mineral dust. $SO_4^{2-}$ preserved in glacier ice therefore records not only changes in atmospheric sulfur but also its transfer to snow and subsequent preservation.

Modern observations show pronounced spatial and seasonal contrasts in aerosol loading across the TP. Northern and western regions receive mineral dust and transported pollution, whereas the southern margins are influenced by South Asian emissions, monsoon transport, and wet removal (Zhu et al., 2019; Bian et al., 2020). Mineral dust further complicates the sulfur cycle because $SO_4^{2-}$ can be transported with mineral particles or formed through heterogeneous reactions on dust surfaces (Bauer and Koch, 2005). These contemporary observations constrain sources and transport pathways, but their duration is too short to resolve multidecadal regional change.

Ice cores extend this perspective across decades to centuries. Records from the northern, interior, and southern TP document distinct histories of $SO_4^{2-}$ and related ions (Thompson et al., 1990, 2000, 2018; Zhao et al., 2011; Wang et al., 2019). A direct comparison of northwestern and southeastern ice cores further linked contrasting glaciochemical trends to westerly and monsoon source regimes (Yang et al., 2022). Together, these studies establish strong site and circulation dependence, but they span different periods, resolutions, and accumulation environments. It therefore remains unclear whether historical $SO_4^{2-}$ trends share a common sign across the TP or differ among regions.

Coupled Model Intercomparison Project Phase 6 (CMIP6) simulations provide a complementary test of the historical $SO_4^{2-}$ cycle (Turnock et al., 2020). Moseid et al. (2022) compared deposition-derived $SO_4^{2-}$ concentrations with ice-core records across nine global regions and found that models reproduced trend direction more consistently than concentration magnitude, while performing poorly over high mountain terrain. The TP is a stringent regional test because steep relief, mineral dust, monsoon–westerly interactions, and strong precipitation gradients can produce opposing local trajectories even under a common large-scale emission history. A Plateau-wide mean can therefore conceal the central model-evaluation question: whether models place $SO_4^{2-}$ increases and decreases in the correct regions.

Here we ask whether the regional organization of TP ice-core $SO_4^{2-}$ is reproduced by 11 CMIP6 models. We group 13 ice cores into six geographic clusters defined by the major mountain ranges of the TP, examine paired $SO_4^{2-}$ and $Ca^{2+}$ records for evidence of spatially variable dust-related influence, and compare the archive with modeled $SO_4^{2-}$ aerosol mass mixing ratio (mmrso4), total $SO_4^{2-}$ deposition, and a precipitation-scaled ice-core flux proxy. The 11-model benchmark establishes the common modeled response. We then use the Community Earth System Model version 2 with the Whole Atmosphere Community Climate Model version 6 (CESM2-WACCM) for detailed single-model analyses.

## 2 Data and Methods

### 2.1 Ice core and emission inventory data

We compiled published $SO_4^{2-}$ records from 13 ice cores across the TP (Table 1; Figure 1). The cores were grouped

https://doi.org/10.5194/egusphere-2026-6745
Preprint. Discussion started: 17 November 2026
© Author(s) 2026. CC BY 4.0 License.

into six geographic clusters, each corresponding to a major mountain range or physiographic cluster of the TP. NW1 and NE1 lie along the northern band of the network, in the northwest and northeast, respectively. MD1–MD3 lie along the middle band and are numbered from west to east, whereas SO1 lies on the southern margin. NW1 comprises the Muztagata1 and Muztagata3 cores from the eastern Pamir, and NE1 comprises the Dunde core from the Qilian Mountains. MD1 comprises the Guliya and Chongce cores from the West Kunlun Mountains, together with the Aru core from the adjacent northwestern TP. MD2 comprises the Zangserkangri and QT1 cores from the Qiangtang Plateau in the interior TP. MD3 comprises the Geladandong, Guoqu, and XiaoDongkemadi cores from the Tanggula Mountains. SO1 comprises the Dasuopu and Rongbuk cores from the central Himalayas. Sect. 2.3 describes the regional averaging procedure. Paired $SO_4^{2-}$ and $Ca^{2+}$ records are available for only nine cores (Muztagata3, Guliya, Chongce, Zangserkangri, QT1, Geladandong, XiaoDongkemadi, Dasuopu, and Rongbuk).

Anthropogenic emissions of sulfur dioxide ($SO_2$) and other reactive gases and aerosol precursors were obtained from the Community Emissions Data System (CEDS; Hoesly et al., 2018), release v_2021_04_21, an updated and improved version of the CEDS inventory used for CMIP6. Historical biomass-burning emissions were taken from a separate CMIP6 input dataset (van Marle et al., 2017).

We used four model diagnostics: the $SO_4^{2-}$ aerosol mass mixing ratio, dry $SO_4^{2-}$ deposition (dryso4), wet $SO_4^{2-}$ deposition (wetso4), and precipitation (pr). Neither deposition variable is separated by sulfur source in the model output.

**Table 1. Ice-core records over the Tibetan Plateau used in this study.**

| Name | Location and elevation | Region | Time coverage | Source |
|---|---|---|---|---|
| Muztagata1 | 38.28°N, 75.02°E, 6350m | NW1 | 1957–2000 | Liu et al. (2008) |
| Muztagata3 | 38.28°N, 75.10°E, 7010m | NW1 | 1907–2002 | Zhao et al. (2011) |
| Dunde | 38.10°N, 96.40°E, 5325m | NE1 | 1850–1990 | Thompson et al. (1990) |
| Guliya | 35.23°N, 84.46°E, 6200m | MD1 | 1850–2014 | Thompson et al. (2018) |
| Aru | 33.99°N, 82.26°E, 6150m | MD1 | 1850–2016 | Yang et al. (2024) |
| Chongce | 35.23°N, 81.12°E, | MD1 | 1903–1992 | E et al. (2016) |

https://doi.org/10.5194/egusphere-2026-6745
Preprint. Discussion started: 17 November 2026
© Author(s) 2026. CC BY 4.0 License.

| | | | | |
|---|---|---|---|---|
| | 6530m | | | |
| Zangserkangri | 34.30°N, 85.85°E, 6226m | MD2 | 1951–2008 | Zou et al. (2020) |
| QT1 | 33.30°N, 88.69°E, 5890m | MD2 | 1850-2011 | Wang et al. (2019) |
| XiaoDongkemadi | 33.07°N, 92.08°E, 5700m | MD3 | 1927–2006 | Li et al. (2015) |
| Geladandong | 33.58°N, 91.18°E, 5750m | MD3 | 1850-1982 | Zhang et al. (2016) |
| Guoqu | 33.58°N, 91.18°E, 5720m | MD3 | 1935-2004 | Grigholm et al. (2009) |
| Dasuopu | 28.38°N, 85.72°E, 7200m | SO1 | 1850-1996 | Thompson et al. (2000); Duan et al. (2007) |
| Rongbuk | 27.98°N, 86.92°E, 6450m | SO1 | 1850-1997 | Qin et al. (2002) |

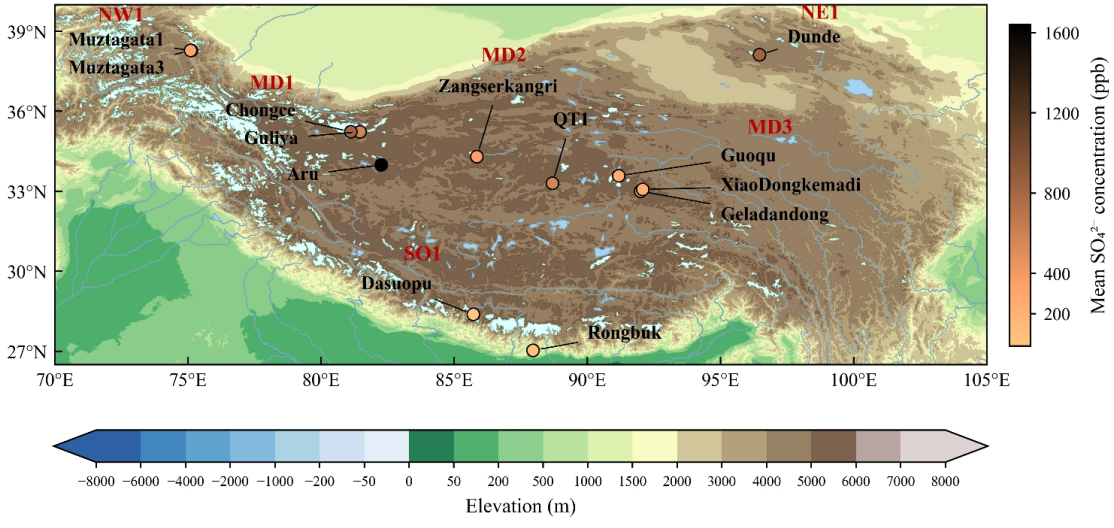



**Figure 1.** Locations of the 13 ice-core sites on the Tibetan Plateau and their mean observed $SO_4^{2-}$ concentrations.

https://doi.org/10.5194/egusphere-2026-6745
Preprint. Discussion started: 17 November 2026
© Author(s) 2026. CC BY 4.0 License.

Marker colors indicate the arithmetic mean concentration (ppb) over each site's specific observation period listed in Table 1, calculated using annual records except for the decadal Dunde record. The records collectively span 1850–2016, with no common averaging period imposed. Site labels and regional groupings follow Table 1. Background shading shows elevation from the ETOPO 2022 ice-surface model (MacFerrin et al., 2025).

### 2.2 CMIP6 historical simulations

We used historical simulations from 11 CMIP6 models to compare modeled $SO_4^{2-}$ with the ice-core records. The CMIP6 historical experiment applies coordinated time-varying forcings from 1850 to 2014 (Eyring et al., 2016). The multi-model time series of mmrso4 and total $SO_4^{2-}$ deposition (Sect. 3.2) use their common 1850–2005 interval.

We analyzed mmrso4, dry and wet $SO_4^{2-}$ deposition (dryso4 and wetso4), and precipitation (pr). At each regional cluster, mmrso4 was sampled from the model level closest to the pressure estimated for the cluster elevation. Dry and wet deposition were summed to obtain total modeled $SO_4^{2-}$ deposition. Precipitation was used to scale ice-core $SO_4^{2-}$ concentrations to a flux proxy.

The ensemble comprises IPSL-CM5A2-INCA, IPSL-CM6A-LR-INCA, MIROC-ES2L, MIROC6, UKESM1-0-LL, MPI-ESM-1-2-HAM, MRI-ESM2-0, GISS-E2-1-H, CESM2, CESM2-FV2, and CESM2-WACCM. These models span different aerosol and atmospheric-chemistry frameworks, resolutions, vertical domains, and degrees of Earth-system coupling (Sepulchre et al., 2020; Boucher et al., 2020; Hajima et al., 2020; Tatebe et al., 2019; Sellar et al., 2019; Mauritsen et al., 2019; Tegen et al., 2019; Yukimoto et al., 2019; Kelley et al., 2020; Danabasoglu et al., 2020; Gettelman et al., 2019; Emmons et al., 2020).

CESM2-WACCM was used for the detailed single-model analyses because it provides a comprehensive vertically resolved interactive chemistry framework and detailed aerosol treatment (Gettelman et al., 2019; Emmons et al., 2020). It also shows relatively good agreement with the observed regional precipitation patterns among the 11 models evaluated here (Text S1 and Table S1). The ensemble member used for each model and variable is listed in Table S2.

### 2.3 Data processing and model comparison

To compare records with different concentration ranges, we standardized each ion time series relative to a site-specific reference period. For anomaly figures, the standardized value was calculated as:

$$Z_i(t) = \frac{C_i(t) - \overline{C}_{i,\mathrm{ref}}}{\sigma_{i,\mathrm{ref}}} \quad (1)$$

where $C_i(t)$ is the measured concentration for site i at year t, $\overline{C}_{i,\mathrm{ref}}$ and $\sigma_{i,\mathrm{ref}}$ are the mean and standard deviation during the 1900-1950 reference period. This period is used as an early-industrial baseline rather than a strictly preindustrial state. Trend interpretations are based on the raw concentration and flux records, while standardized series are used only to compare relative variability among sites. At the nine sites with paired records, same-time-step $SO_4^{2-}$-$Ca^{2+}$ covariation was summarized using Spearman's rank correlation. Dasuopu was evaluated at the decadal resolution of the available paired series.

https://doi.org/10.5194/egusphere-2026-6745
Preprint. Discussion started: 17 November 2026
© Author(s) 2026. CC BY 4.0 License.

For the emission inventory comparison (Sect. 3.1.1), each regional time series was normalized relative to the 1850-1900 mean to highlight changes in emissions after the early historical period. For ice-core records with shorter temporal coverage, concentration anomalies were calculated relative to the pre-1950 or 1900-1950 reference interval where data allowed. Because broad regional emissions do not necessarily represent the air masses reaching each glacier, these comparisons are interpreted as first-order source-region context rather than a formal attribution. A trajectory-weighted emission index would be needed for quantitative source attribution.

To visualize the spatial pattern of $SO_4^{2-}$ trend estimates, we used Radial Basis Function (RBF) interpolation. Because the network contains only 13 unevenly distributed ice cores, the interpolated fields are used only to illustrate first-order spatial contrasts. Quantitative interpretation is therefore restricted to individual sites and the six regional clusters.

Ice-core $SO_4^{2-}$ flux $F_{SO_4^{2-}}$ (mg $m^{-2}$ $yr^{-1}$) was calculated as

$$F_{SO_4^{2-}} = \frac{C_{SO_4^{2-}} \times A}{1000} \quad (2)$$

where $C_{SO_4^{2-}}$ is the $SO_4^{2-}$ concentration (μg $L^{-1}$) and A is the annual accumulation (mm w.e. $yr^{-1}$).

Modeled $SO_4^{2-}$ deposition flux (mg $m^{-2}$ $yr^{-1}$) was calculated as

$$F_{\mathrm{dep}} = \left(D_{\mathrm{dry}} + D_{\mathrm{wet}}\right) \times 10^6 \times \Delta t_{\mathrm{yr}} \quad (3)$$

where $D_{\mathrm{dry}}$ and $D_{\mathrm{wet}}$ correspond to the CMIP6 variables dryso4 and wetso4 (kg $m^{-2}$ $s^{-1}$).

The precipitation-scaled ice-core $SO_4^{2-}$ flux is an archive-based proxy rather than an independent measurement of atmospheric deposition. It is therefore used to compare regional signs and spatial organization, whereas modeled dry and wet deposition are evaluated as model diagnostics.

Annual regional ice-core series were calculated as the arithmetic mean of the records available in each year, with equal weight assigned to each contributing core and no interpolation across missing ice-core years. A regional year was retained when at least one core was available. Smoothed curves are shown only for visualization: annual series use a centered 10-observation running mean, whereas the decadal NE1 series uses a centered two-observation mean. All reported correlations and early-to-late changes were calculated from the unsmoothed data.

## 3 Results

### 3.1 Ice-core-based $SO_4^{2-}$ variability over the Tibetan Plateau

#### 3.1.1 Temporal evolution of $SO_4^{2-}$ concentrations

To characterize the temporal evolution of $SO_4^{2-}$ preserved in TP glaciers, we analyzed the $SO_4^{2-}$ records from the 13 ice cores (Figure 1; Figure S1), aggregated into the six geographic clusters defined in Sect. 2.1 (Table 1). Regional $SO_4^{2-}$ series were calculated from the available records within each cluster, and interpretations involving $Ca^{2+}$ were restricted to the nine sites with paired measurements.

https://doi.org/10.5194/egusphere-2026-6745
Preprint. Discussion started: 17 November 2026
© Author(s) 2026. CC BY 4.0 License.

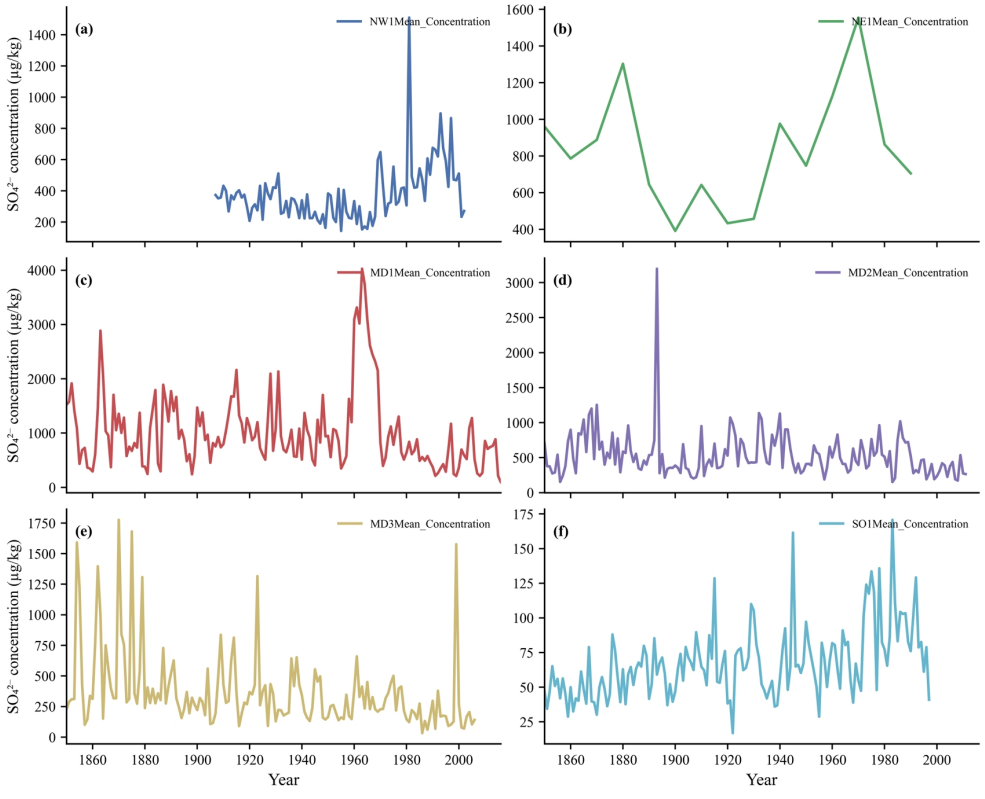



**Figure 2.** Temporal trends in $SO_4^{2-}$ concentrations for (a) NW1, (b) NE1, (c) MD1, (d) MD2, (e) MD3, and (f) SO1 across the Tibetan Plateau.

The regional $SO_4^{2-}$ series differ in their temporal evolution (Figure 2). All clusters show interannual to decadal variability, and several contain short-lived peaks. In NW1, $SO_4^{2-}$ concentrations show a modest decline prior to ~1960, followed by a steadily increasing trend in the subsequent decades. The NE1 record, although based on fewer observations, exhibits relatively low concentrations from 1900 to 1940 with a broad peak around the 1970s. MD1 and MD2 are characterized by prominent peaks around ~1965 and ~1890, respectively, superimposed on otherwise relatively stable backgrounds. In both regions, beyond these episodic maxima, no clear persistent long-term increasing or decreasing trend is evident. MD3 shows relatively high and variable concentrations in the 19th century, followed by a general reduction in peak magnitude and an overall downward tendency during the 20th century. The southernmost region SO1, maintains consistently low $SO_4^{2-}$ levels throughout the record but exhibits a gradual increase over time. Together, these regionally aggregated records highlight strong temporal heterogeneity across the six clusters.

https://doi.org/10.5194/egusphere-2026-6745
Preprint. Discussion started: 17 November 2026
© Author(s) 2026. CC BY 4.0 License.

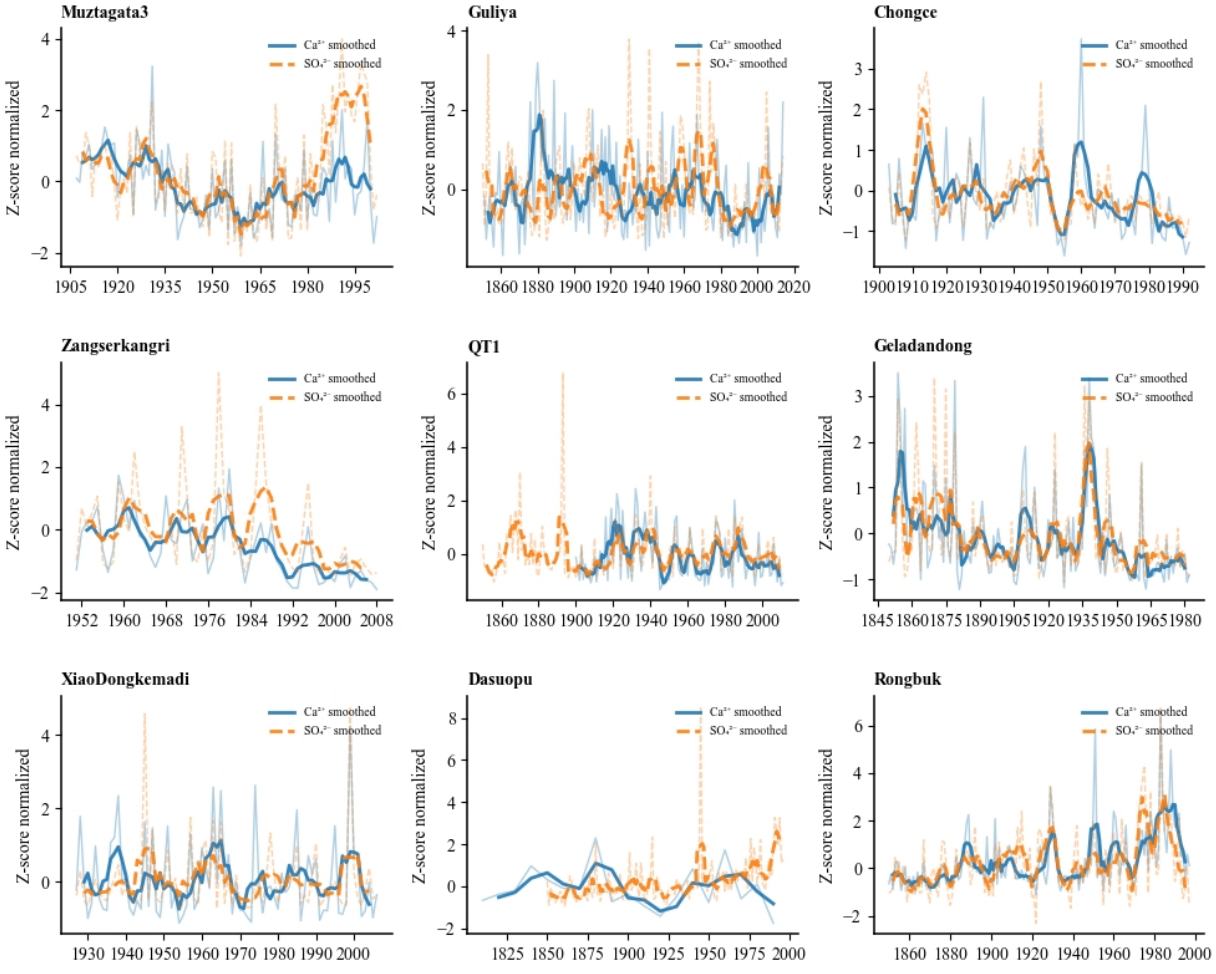



**Figure 3.** Normalized Z-score time series of $Ca^{2+}$ and $SO_4^{2-}$ concentrations at various ice core sites across the Tibetan Plateau, highlighting the temporal trends and smoothed data.

Figure 3 compares $SO_4^{2-}$ and $Ca^{2+}$ at the nine cores where both ions are available. The two ions covary strongly at seven sites (Spearman's $\rho = 0.71–0.85$), whereas Guliya ($\rho = 0.04$) and Dasuopu ($\rho = 0.03$; 15 decadal observations) show little overall association. At Muztagata3, the correlation is similar before and after 1960 ($\rho =$ 0.80 and 0.83), so $SO_4^{2-}$ there remains coupled to $Ca^{2+}$ during the post-1960 increase in NW1.These site-to-site differences are consistent with spatially variable dust-related contributions to $SO_4^{2-}$, although $SO_4^{2-}$–$Ca^{2+}$ covariation alone cannot uniquely identify $SO_4^{2-}$ sources.

https://doi.org/10.5194/egusphere-2026-6745
Preprint. Discussion started: 17 November 2026
© Author(s) 2026. CC BY 4.0 License.

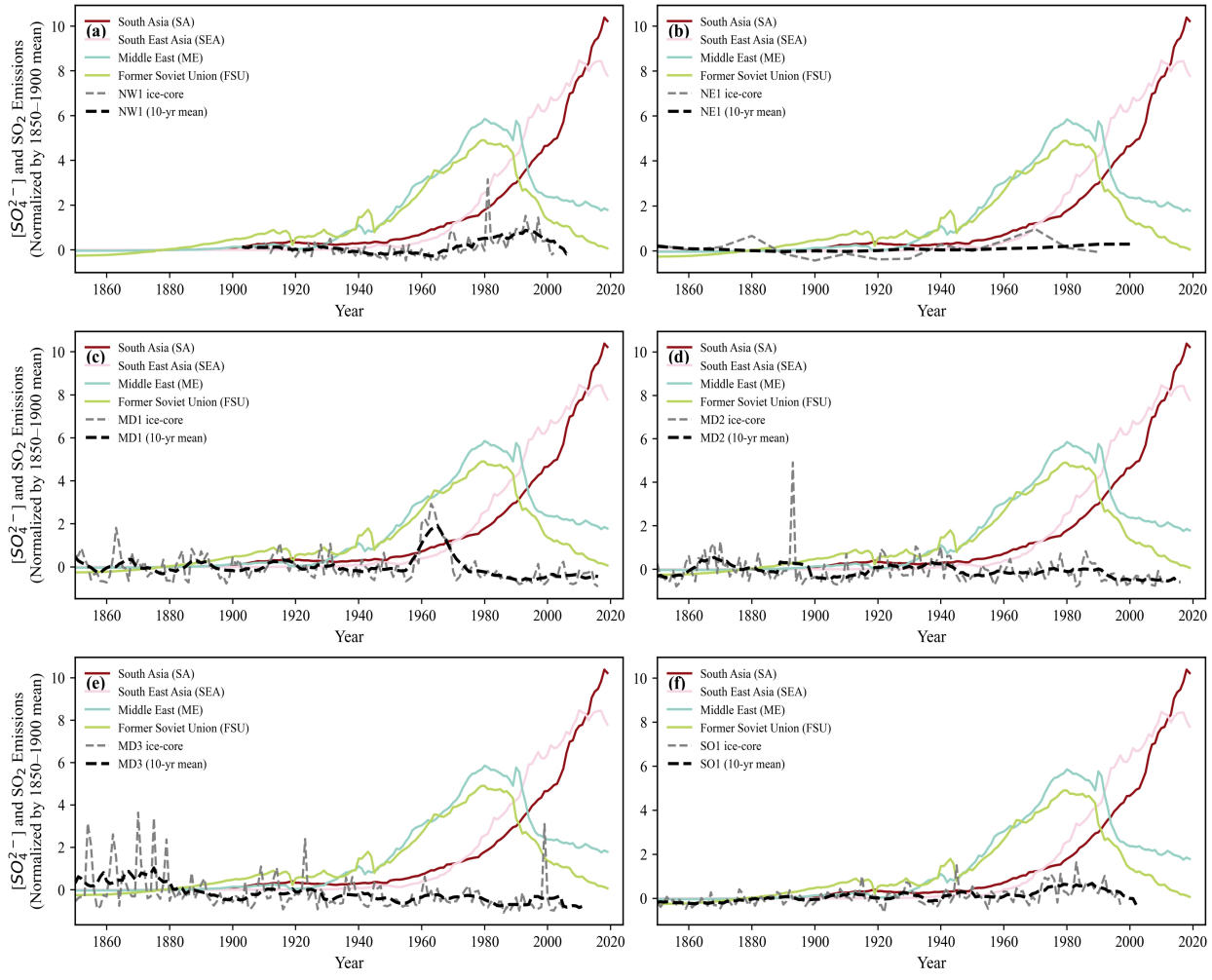



**Figure 4.** Comparison of normalized emissions of $SO_2$ and $SO_4^{2-}$ from South Asia, Southeast Asia, the Middle East, and the Former Soviet Union with ice core data from regions (a) NW1, (b) NE1, (c) MD1, (d) MD2, (e) MD3, and (f) SO1. The black dashed lines represent the smoothed 10-year moving averages for each dataset.

Figure 4 places the regional ice-core $SO_4^{2-}$ series alongside $SO_2$ and $SO_4^{2-}$ emissions from surrounding source regions. The increases in NW1 and SO1 broadly coincide with rising emissions in several upwind regions, whereas MD1, MD2, and MD3 show weaker or negative changes. NE1 shows limited correspondence. The comparison suggests that regional emissions contribute to the marginal increases, while transport and deposition processes modify the signal reaching individual glaciers.

### 3.1.2 Spatial pattern of $SO_4^{2-}$ concentration trends

The spatial distribution of mean $SO_4^{2-}$ concentrations based on the 13 ice cores (Figure 1) shows a northwest–southeast gradient across the Tibetan Plateau, with higher concentrations in the westerly-influenced northern and

https://doi.org/10.5194/egusphere-2026-6745
Preprint. Discussion started: 17 November 2026
© Author(s) 2026. CC BY 4.0 License.

western regions and substantially lower values toward the monsoon-dominated southeast. To describe the spatial pattern of change, early- and late-period regional means were compared as:

$$R = \frac{\overline{C}_{\text{late}} - \overline{C}_{\text{early}}}{\overline{C}_{\text{early}}} \times \frac{100}{\Delta t} \quad (4)$$

The early and late periods are 1900–1950 and 1950–2000 for most regions; NE1 uses 1850–1900 and 1950–2000.

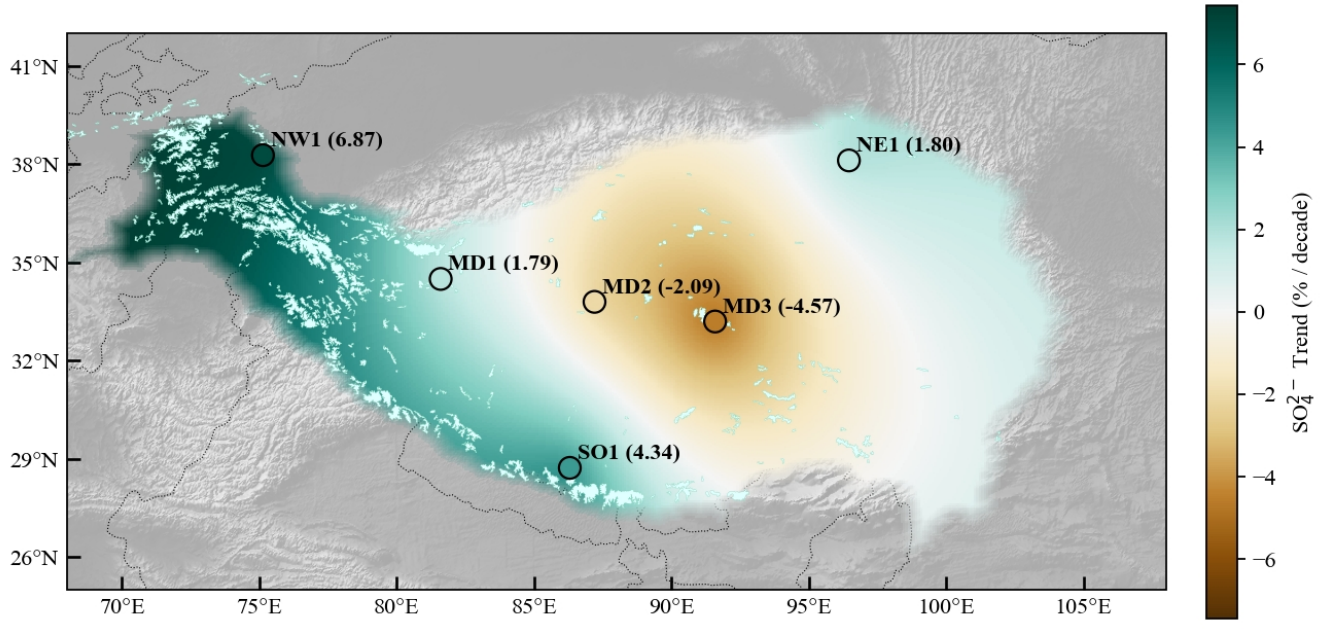



**Figure 5**. Spatial trends of $SO_4^{2-}$ concentration changes over the Tibetan Plateau.

The largest positive change occurs in NW1 (6.87 % decade$^{-1}$; Figure 5), followed by SO1 (4.34 % decade$^{-1}$). NE1 and MD1 show smaller positive changes of 1.80 and 1.79 % decade$^{-1}$, respectively, while MD2 and MD3 show negative changes of −2.09 and −4.57 % decade$^{-1}$. The pattern indicates stronger increases near parts of the Plateau margin and weaker or negative changes in the interior. The RBF interpolation visualizes this margin-interior contrast, but the sparse and uneven ice-core network does not support quantitative interpretation of fine-scale gradients. Therefore, the robust result is the contrast among site clusters rather than the exact gridded spatial field.

### 3.1.3 Reconstructed $SO_4^{2-}$ fluxes from ice cores

To compare the ice-core records on a common area basis, we calculated precipitation-scaled $SO_4^{2-}$ fluxes using CESM2-WACCM precipitation at the ice-core locations:

https://doi.org/10.5194/egusphere-2026-6745
Preprint. Discussion started: 17 November 2026
© Author(s) 2026. CC BY 4.0 License.

$$F_{\text{ice}} = \frac{C_{SO_4^{2-}} P_{\text{model}}}{1000} \quad (5)$$

Where $C_{SO_4^{2-}}$ is the measured $SO_4^{2-}$ concentration (μg $L^{-1}$) and $P_{\text{model}}$ is the CESM2-WACCM annual precipitation (mm $yr^{-1}$). The resulting fluxes have units of mg $m^{-2}$ $yr^{-1}$ and combine measured ice-core $SO_4^{2-}$ concentrations with modeled precipitation to provide a consistent basis for regional comparison.

Wet deposition exceeds dry deposition in most regions of the CMIP6 simulations (Figure S2; Figure S3). The precipitation products shown in Figure S4 exhibit no consistent long-term change across the sampled sites. Precipitation changes are therefore unlikely to explain the contrasting regional $SO_4^{2-}$-flux trends. Results based on alternative precipitation products are given in Text S1.

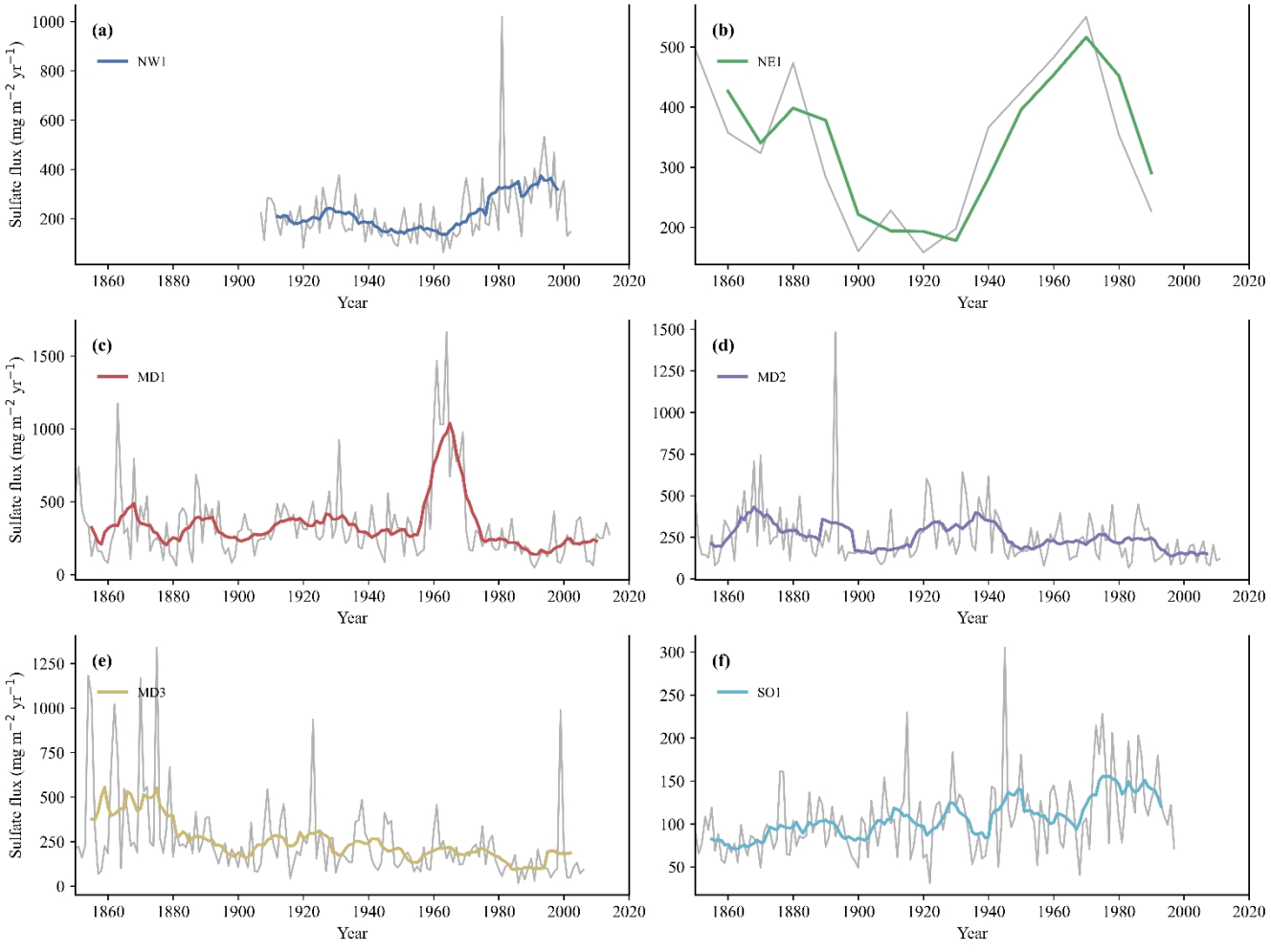



**Figure 6.** Regional $SO_4^{2-}$ flux calculated from ice-core $SO_4^{2-}$ concentration and CESM2-WACCM precipitation for (a) NW1, (b) NE1, (c) MD1, (d) MD2, (e) MD3, and (f) SO1. Gray lines show the original time series and

https://doi.org/10.5194/egusphere-2026-6745
Preprint. Discussion started: 17 November 2026
© Author(s) 2026. CC BY 4.0 License.

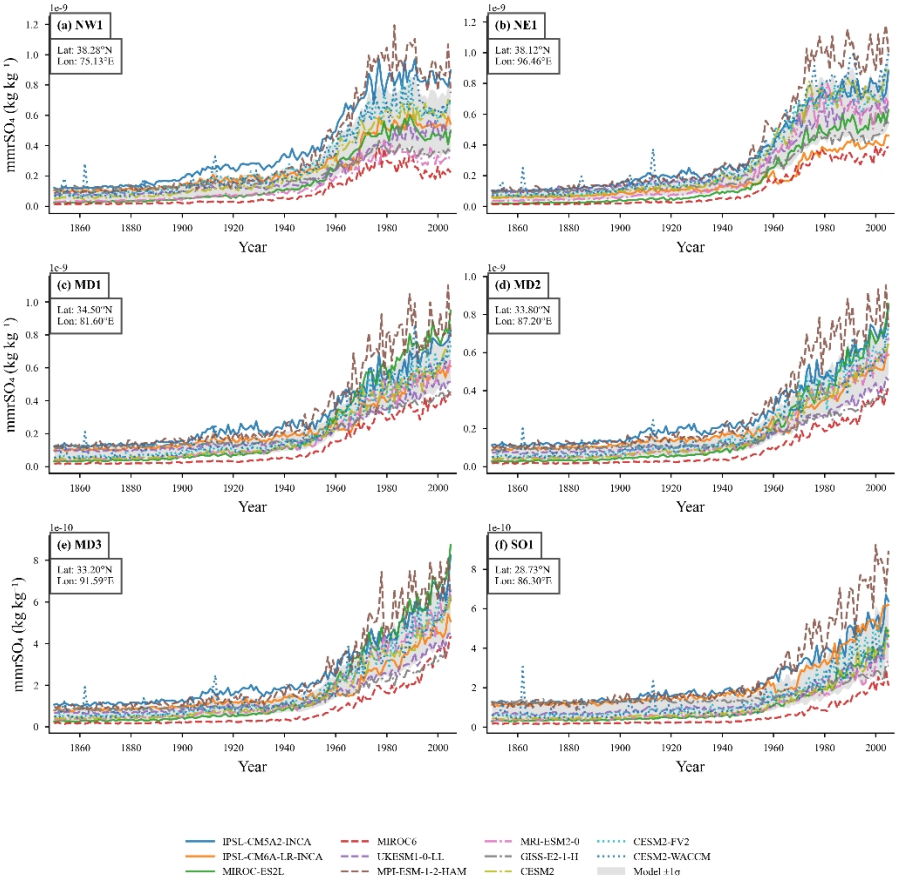
colored lines show the smoothed regional series.

The reconstructed $SO_4^{2-}$ fluxes (Figure 6) retain the heterogeneous regional pattern observed in the concentration records. NW1 shows a marked increase after approximately 1960 following a relatively stable earlier period. NE1 shows no clear monotonic trend and has a shorter and more variable record. MD1 and MD2 remain broadly stable, whereas MD3 has lower twentieth-century fluxes than nineteenth-century values. SO1 exhibits a weak but sustained increase. Overall, these reconstructions support the concentration-based pattern of stronger $SO_4^{2-}$ increases at the Plateau margins, while interior regions remained relatively stable or declined.

## 3.2 Model-based $SO_4^{2-}$ deposition over the Tibetan Plateau

### 3.2.1 Modeled $SO_4^{2-}$ concentrations at ice-core cluster elevations

For comparison with the ice-core records, mmrso4 from CMIP6 models were extracted at pressure levels approximating each cluster elevation. The mmrso4 variable represents $SO_4^{2-}$ aerosol mass mixing ratio in air, while dryso4 and wetso4 represent surface deposition rates. The mmrso4 comparison evaluates modeled $SO_4^{2-}$ abundance near glacier elevations, and the wetso4 + dryso4 comparison evaluates modeled deposition.



https://doi.org/10.5194/egusphere-2026-6745
Preprint. Discussion started: 17 November 2026
© Author(s) 2026. CC BY 4.0 License.

**Figure 7**. CMIP6-simulated $SO_4^{2-}$ mass mixing ratios ($mmrSO_4$) at pressure levels corresponding to cluster site elevations for (a) NW1, (b) NE1, (c) MD1, (d) MD2, (e) MD3, and (f) SO1. Individual lines represent different CMIP6 models, and the shaded envelopes denote the inter-model spread (±1σ).

Figure 7 shows the simulated $SO_4^{2-}$ mass mixing ratios near the elevations of the six ice-core regions. Most models maintain relatively low values during the nineteenth and early twentieth centuries and rise more rapidly after the mid-twentieth century. The magnitude and timing of the increase vary among models and regions, but the simulations generally show greater spatial coherence than the ice-core records.

### 3.2.2 Spatial patterns in modeled $SO_4^{2-}$ concentrations

We used CESM2-WACCM to examine the spatial pattern of modeled $SO_4^{2-}$ change across the Tibetan Plateau (Figure 8). For each grid cell and regional cluster, we calculated the difference between mean $SO_4^{2-}$ aerosol mass mixing ratios for 1950–1999 and 1900–1949, normalized it by the 1900–1949 mean, and divided by five decades. The resulting early-to-late relative change rate is expressed in % $decade^{-1}$ and provides a common measure of $SO_4^{2-}$ change between the two 50-year periods.

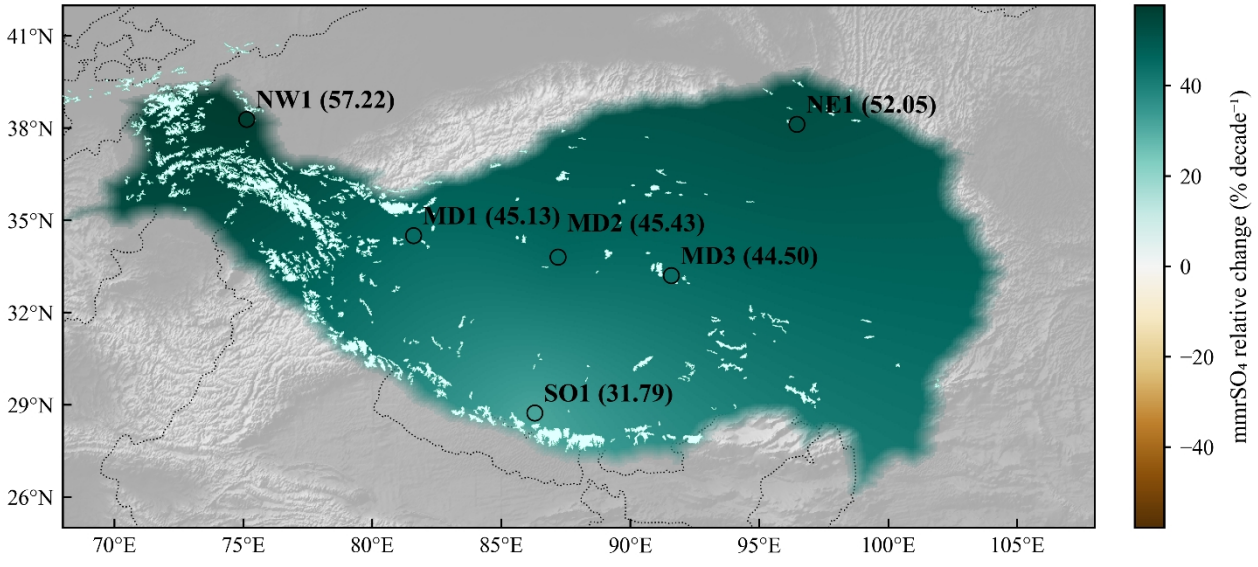



**Figure 8**. Early-to-late relative change rate in CESM2-WACCM $SO_4^{2-}$ aerosol mass mixing ratio (mmrso4) from 1900–1949 to 1950–1999. The relative difference between the two 50-year means is normalized by five decades and expressed in % $decade^{-1}$. Circles mark the six regional ice-core clusters, and labels show the corresponding regional values.

CESM2-WACCM simulates increases in $SO_4^{2-}$ aerosol mass mixing ratio across all six regions. The rates are 31.79 % $decade^{-1}$ in SO1, 57.22 % $decade^{-1}$ in NW1, 52.05 % $decade^{-1}$ in NE1, 45.13 % $decade^{-1}$ in MD1,

https://doi.org/10.5194/egusphere-2026-6745
Preprint. Discussion started: 17 November 2026
© Author(s) 2026. CC BY 4.0 License.

45.43 % decade$^{-1}$ in MD2, and 44.50% decade$^{-1}$ in MD3. The regional range is 25.43 percentage points, indicating that the modeled differences are primarily in magnitude rather than direction. This spatially coherent increase contrasts with the ice-core records, where positive changes are concentrated mainly along parts of the Plateau margin, while several interior clusters remain stable or decline.

### 3.2.3 Modeled $SO_4^{2-}$ deposition fluxes

Figure 9 shows total $SO_4^{2-}$ deposition from the 11 CMIP6 models. Across the six regional clusters, most simulations show relatively low $SO_4^{2-}$ deposition during the nineteenth and early twentieth centuries, followed by a more pronounced increase after the mid-twentieth century. The magnitude of this increase varies substantially among both models and regions. NW1, NE1, MD1, and MD2 generally show sustained increases through the latter half of the twentieth century, whereas MD3 tends to exhibit smaller absolute deposition and a weaker increase. SO1 has the largest simulated deposition and the widest inter-model spread, particularly during the late twentieth century.

Despite these regional differences in magnitude, the modeled deposition series exhibit a broadly coherent temporal evolution, with increasing $SO_4^{2-}$ deposition after approximately 1950 in most regions and models. This behavior contrasts with the ice-core-derived $SO_4^{2-}$ fluxes, which show stronger regional heterogeneity, including pronounced increases at some Plateau-margin regions but weak, stable, or declining changes in several interior clusters. The models therefore simulate a twentieth-century increase in every cluster, whereas the ice-core flux proxy shows weak or negative changes in the interior clusters.

https://doi.org/10.5194/egusphere-2026-6745
Preprint. Discussion started: 17 November 2026
© Author(s) 2026. CC BY 4.0 License.

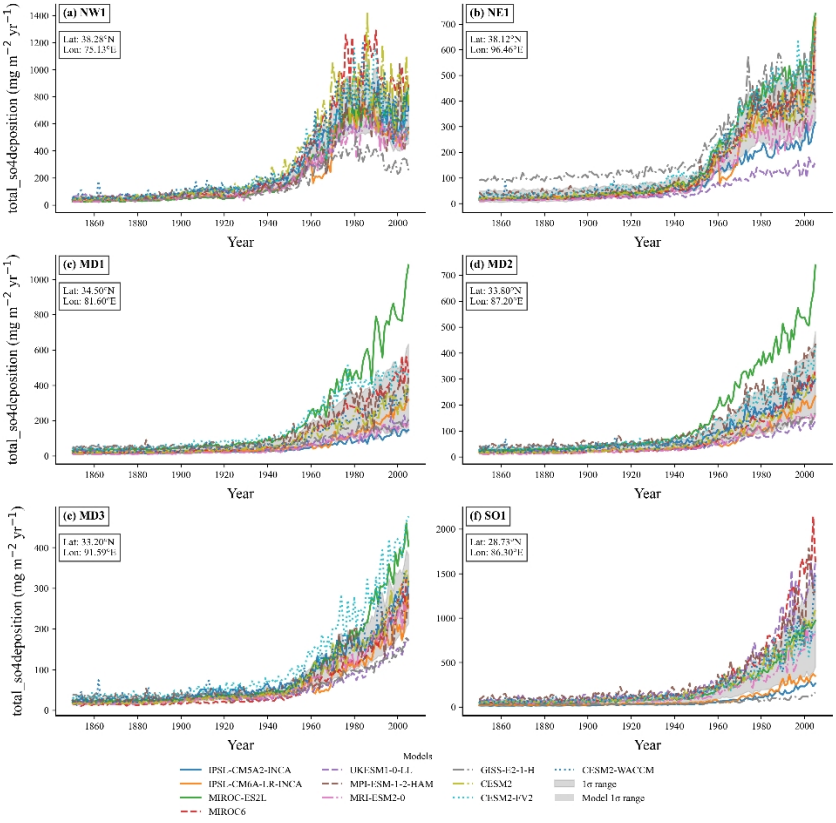



**Figure 9**. Total $SO_4^{2-}$ deposition (dryso4 + wetso4; mg $m^{-2}$ $yr^{-1}$) simulated by the 11 CMIP6 models for (a) NW1, (b) NE1, (c) MD1, (d) MD2, (e) MD3, and (f) SO1. Lines show individual models.

## 4 Discussion.

Arctic ice-core records provide important evidence of anthropogenic perturbations to the sulfur cycle. Records from Greenland and Svalbard show a general increase in non-sea-salt $SO_4^{2-}$ from the late 19th century to the 1970s, followed by a marked decline (Iizuka et al., 2022). Previous studies have also shown that CMIP6 models reproduce the broad timing and direction of twentieth-century $SO_4^{2-}$ changes in the Arctic to some extent, although the magnitude of the changes varies among regions and models (Moseid et al., 2022).

In contrast, $SO_4^{2-}$ records over the Tibetan Plateau are influenced by multiple processes, including natural dust inputs, long-range anthropogenic transport, regional atmospheric circulation, and high-elevation deposition. Building on the model–ice-core comparison framework used in Arctic studies, we compare multiple TP ice-core records with CMIP6 simulations at the regional scale. The results show that TP ice-core $SO_4^{2-}$ exhibits pronounced regional differences in both temporal evolution and spatial behavior, whereas the models generally simulate more coherent changes, highlighting model–observation discrepancies.

### 4.1 Temporal discrepancies between ice cores and models

https://doi.org/10.5194/egusphere-2026-6745
Preprint. Discussion started: 17 November 2026
© Author(s) 2026. CC BY 4.0 License.

The ice-core records do not follow a single Plateau-wide trajectory. NW1 rises after approximately 1960, NE1 contains a broad late-twentieth-century maximum, MD1 and MD2 include pronounced episodic peaks, MD3 declines from higher nineteenth-century values, and SO1 increases gradually. These differences point to regional variation in sources, transport, deposition, and preservation.

The CMIP6 $SO_4^{2-}$ series show a common temporal structure, with relatively weak early variation followed by stronger increases after the mid-twentieth century (Fig. 7). Model spread increases during the later period, indicating differences in simulated magnitude, while the direction of change remains more coherent than in the ice cores.

The paired $SO_4^{2-}$ and $Ca^{2+}$ records provide additional context for this spatial heterogeneity. Strong covariation at seven of the nine sites is consistent with a substantial dust-related $SO_4^{2-}$ contribution, whereas Guliya and Dasuopu show relatively weak overall associations. These site-dependent relationships indicate that the relative importance of dust-related and non-dust influences varies across the Plateau and may contribute to the heterogeneous ice-core histories.

### 4.2 Spatial contrasts between ice cores and models

The ice-core records show both a northwest–southeast concentration gradient and a distinct margin-to-interior contrast in temporal change (Figure 1; Figure 5). Higher mean $SO_4^{2-}$ concentrations in the northwest are consistent with stronger influence from the mid-latitude westerlies and dust transport, whereas lower concentrations in the south occur in regions more strongly affected by the Indian summer monsoon. In particular, the relatively high $SO_4^{2-}$ concentrations in the northwestern Plateau may partly reflect the contribution of dust-associated $SO_4^{2-}$ transported by the westerlies, while stronger wet removal in the southern and southeastern Plateau may contribute to lower background concentrations.

The temporal changes further emphasize the regional character of the ice-core records. NW1 and SO1 show the clearest positive changes, suggesting enhanced $SO_4^{2-}$ input during the later part of the records in some marginal regions of the Plateau. In contrast, the interior clusters show much weaker changes, with MD2 and especially MD3 exhibiting little increase or an overall decline. The simultaneous decreases in $SO_4^{2-}$ and $Ca^{2+}$ observed in some paired records suggest that changes in dust supply may have contributed to the declining $SO_4^{2-}$ signal in the interior. However, the relative roles of dust abundance, $SO_4^{2-}$ formation on mineral particles, atmospheric transport, and wet removal cannot be separated using the ice-core records alone. Changes in glacier accumulation may also influence the preserved concentration signal, although the available precipitation diagnostics do not indicate a uniform long-term change that could readily explain the contrasting regional trends.

CESM2-WACCM simulates positive changes in atmospheric $SO_4^{2-}$ in all six clusters (Figure 8), at rates several times larger than those in the ice cores. It therefore does not reproduce the contrast between increases in NW1 and SO1 and decreases in MD2 and MD3.

The mismatch is consistent with differences in how glacier archives and grid-cell model diagnostics integrate $SO_4^{2-}$ formation, dust-associated $SO_4^{2-}$, transport, scavenging, and surface preservation. The comparison points to dust–$SO_4^{2-}$ chemistry, wet removal over complex terrain, and grid-cell elevation as priorities for process-level

https://doi.org/10.5194/egusphere-2026-6745
Preprint. Discussion started: 17 November 2026
© Author(s) 2026. CC BY 4.0 License.

evaluation.

### 4.3 Discrepancies in $SO_4^{2-}$ fluxes between ice-core reconstructions and CMIP6 simulations

The reconstructed ice-core $SO_4^{2-}$ fluxes preserve the same broad regional organization as the concentration records (Figure 6). Flux increases in NW1 and MD1, increases more gradually in NE1 and SO1, and declines in MD2 and MD3. These regional differences indicate that changes in $SO_4^{2-}$ deposition were not spatially uniform across the Tibetan Plateau.

Figure 10 compares the early-to-late change in the precipitation-scaled ice-core $SO_4^{2-}$ flux proxy with the change in total $SO_4^{2-}$ deposition simulated by CESM2-WACCM. The ice-core proxy is positive in NW1, NE1, MD1, and SO1 but negative in MD2 and MD3, whereas CESM2-WACCM shows increasing total $SO_4^{2-}$ deposition across the displayed Plateau domain. The comparison therefore reinforces the time-series result: the modeled response is spatially coherent, while the glacier archive preserves stronger regional differentiation. Because panel (a) combines measured $SO_4^{2-}$ concentrations with modeled precipitation, it provides a precipitation-scaled representation of the regional $SO_4^{2-}$ flux pattern.

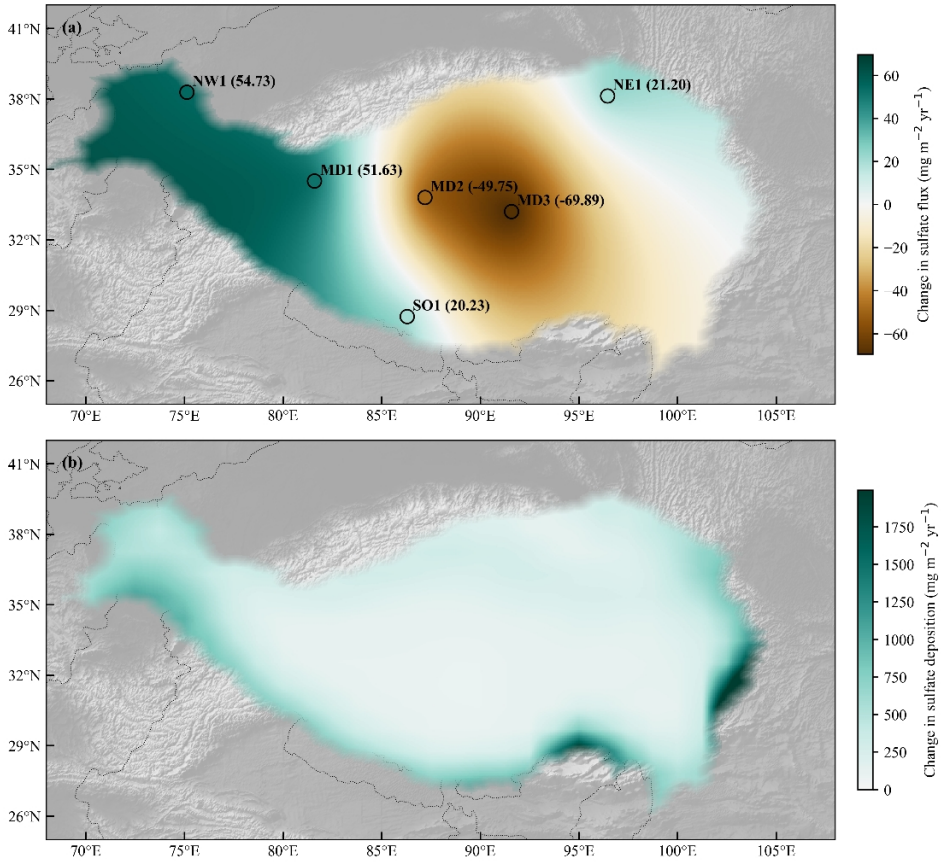



**Figure 10**. Early-to-late changes in $SO_4^{2-}$ flux over the Tibetan Plateau. (a) Precipitation-scaled ice-core $SO_4^{2-}$

https://doi.org/10.5194/egusphere-2026-6745
Preprint. Discussion started: 17 November 2026
© Author(s) 2026. CC BY 4.0 License.

flux calculated with CESM2-WACCM precipitation. NW1, MD1, MD2, MD3, and SO1 compare 1950–1999 with 1900–1949; NE1 compares 1950–1999 with 1850–1899. (b) CESM2-WACCM total $SO_4^{2-}$ deposition (dryso4 + wetso4) for 1951–2000 minus 1900–1950.

Dust-associated $SO_4^{2-}$ is a likely contributor to this contrast. In the interior regions, $SO_4^{2-}$ can be influenced by mineral dust and by heterogeneous $SO_4^{2-}$ formation on alkaline particle surfaces (Bauer and Koch, 2005), which may decouple the ice-core records from the temporal evolution of anthropogenic sulfur emissions. The strong $SO_4^{2-}$ - $Ca^{2+}$ covariation at Chongce, Zangserkangri, QT1, Geladandong, and XiaoDongkemadi supports this interpretation and suggests that dust transport or dust-related chemistry contributes substantially to $SO_4^{2-}$ variability in these regions.

By contrast, marginal regions are more directly exposed to air masses transported from surrounding emission regions and may therefore respond more clearly to large-scale changes in atmospheric sulfur loading. The relative importance of these influences is further modified by the strong topographic gradients of the Tibetan Plateau. Long-range transport into the Plateau interior is constrained by mountain barriers, circulation pathways, and seasonal differences between westerly and monsoon influence. At the same time, wet scavenging can remove $SO_4^{2-}$ efficiently during transport, particularly along regions of enhanced precipitation and orographic uplift. These processes can weaken or redistribute the $SO_4^{2-}$ signal before aerosols reach high-elevation glacier sites.

Glacier records also reflect deposition and preservation processes that are not represented by atmospheric transport alone. Snow accumulation rates, local wind redistribution, sublimation, melt, and post-depositional modification can influence the amount of $SO_4^{2-}$ ultimately preserved in glacier ice. These effects may contribute to differences between individual glacier records and grid-scale model deposition. The contrast between the spatially coherent modeled increase and the more heterogeneous ice-core response therefore likely reflects a combination of source composition, transport, removal, and glacier-specific deposition processes.

The flux comparison thus leads to the same conclusion as the concentration analysis. $SO_4^{2-}$ changes over the Tibetan Plateau depend strongly on region, whereas CESM2-WACCM simulates an increase everywhere. The model and the ice cores disagree in sign in MD2 and MD3, where dust-related processes and complex transport pathways are likely to play a greater role. These ice-core records can therefore serve as a regional constraint on modeled $SO_4^{2-}$ deposition.

### 4.4 Limitations

The ice-core network is sparse and unevenly distributed, and the records differ in length and temporal resolution, so each regional mean reflects the glaciers sampled within it. The flux proxy combines measured concentrations with modeled precipitation and does not account for dry deposition or post-depositional alteration; it is therefore most informative about the sign and spatial pattern of change. Sulfur and oxygen isotopes of $SO_4^{2-}$ ($\delta^{34}S$ and $\Delta^{17}O$) in these cores would help distinguish dust-derived from anthropogenic $SO_4^{2-}$ and identify its formation pathways, providing constraints on the chemical processes represented in the models (Jongebloed et al., 2023).

## 5 Conclusion

https://doi.org/10.5194/egusphere-2026-6745
Preprint. Discussion started: 17 November 2026
© Author(s) 2026. CC BY 4.0 License.

This study combines $SO_4^{2-}$ records from 13 Tibetan Plateau (TP) ice cores with CMIP6 historical simulations to examine the long-term spatial and temporal evolution of $SO_4^{2-}$ over the Plateau. The ice-core records reveal a clear northwest–southeast gradient in mean $SO_4^{2-}$ concentration and pronounced regional differences in temporal evolution. Positive changes since the mid-20th century are concentrated mainly in marginal regions such as NW1 and SO1, whereas several interior regions remain relatively stable or show negative changes, particularly MD3. Paired $SO_4^{2-}$ and $Ca^{2+}$ records further suggest that dust-related processes contribute to part of this spatial heterogeneity.

In contrast, the CMIP6 simulations produce increases in atmospheric $SO_4^{2-}$ and total $SO_4^{2-}$ deposition after the mid-twentieth century in most clusters and models. CESM2-WACCM simulates positive changes in atmospheric $SO_4^{2-}$ in every cluster, at 32–57 % decade$^{-1}$, several times the largest ice-core rate. The models and the ice cores therefore differ in the sign and spatial pattern of long-term change as well as in its magnitude: the models simulate increases across the TP, whereas the ice cores record increases on parts of the margin and declines in parts of the interior.

The comparison points to dust-related $SO_4^{2-}$, wet removal over complex terrain, and the representation of high-elevation grid cells as priorities for model evaluation. $SO_4^{2-}$ deposition biases should not be read directly as biases in $SO_4^{2-}$ radiative forcing, which also depends on aerosol burden, optical properties, and cloud interactions. Sulfur-isotope and mineralogical tracers, trajectory-based source attribution, and source-resolved model diagnostics would help separate the contributions of anthropogenic $SO_2$, dust-related $SO_4^{2-}$, and deposition processes to $SO_4^{2-}$ variability over the TP.

## Code and data availability

Code and data availability The CEDS anthropogenic SO2 emissions analysed here correspond to release v_2021_04_21 (21 April 2021) of the Community Emissions Data System (Hoesly et al., 2018). CMIP6 model output were downloaded from the Earth System Grid Federation; CRU TS4.07 and ERA5 precipitation were obtained from the sources cited in Sect. 2. The ice-core sulfate records were compiled from the published sources cited in Table S3; the original measurements are available from those publications. The compiled site-level annual series, the site coordinates and elevations used for model extraction, and the analysis code are available from the corresponding author upon reasonable request.

## Author contributions

Conceptualization: Lei Geng; Data curation: Dandan Yang, Tandong Yao, Guangjian Wu, Huabiao Zhao, Xiangying Li; Formal analysis: Hongcheng Lu, Peng Wang, Lei Geng; Funding acquisition: Lei Geng; Investigation: Hongcheng Lu, Peng Wang, Lei Geng; Methodology: Hongcheng Lu, Peng Wang, Lei Geng; Project administration: Hongcheng Lu, Lei Geng; Software: Hongcheng Lu, Peng Wang; Writing – original draft: Hongcheng Lu, Peng Wang, Lei Geng; Writing – review & editing: Dandan Yang, Tandong Yao

## Competing interests

The authors declare that they have no conflict of interest.

https://doi.org/10.5194/egusphere-2026-6745
Preprint. Discussion started: 17 November 2026
© Author(s) 2026. CC BY 4.0 License.

**Acknowledgements**

The numerical calculations in this paper have been done on the supercomputing system in the Supercomputing Center of University of Science and Technology of China.

**Financial support**

This research has been supported by the National Natural Science Foundation of China (Grant No. W2411030) and the National Key Research and Development Program of China (Grant No. 2025YFF0811903).

**References**

Bauer, S. E. and Koch, D.: Impact of heterogeneous sulfate formation at mineral dust surfaces on aerosol loads and radiative forcing in the Goddard Institute for Space Studies general circulation model, J. Geophys. Res.-Atmos., 110, D17202, https://doi.org/10.1029/2005JD005870, 2005.

Bian, J., Li, D., Bai, Z., Li, Q., Lyu, D., and Zhou, X.: Transport of Asian surface pollutants to the global stratosphere from the Tibetan Plateau region during the Asian summer monsoon, Natl. Sci. Rev., 7, 516–533, https://doi.org/10.1093/nsr/nwaa005, 2020.

Boucher, O., Servonnat, J., Albright, A. L., Aumont, O., Balkanski, Y., Bastrikov, V., Bekki, S., Bonnet, R., Bony, S., Bopp, L., Braconnot, P., Brockmann, P., Cadule, P., Caubel, A., Cheruy, F., Codron, F., Cozic, A., Cugnet, D., D'Andrea, F., Davini, P., de Lavergne, C., Denvil, S., Deshayes, J., Devilliers, M., Ducharne, A., Dufresne, J.-L., Dupont, E., Éthé, C., Fairhead, L., Falletti, L., Flavoni, S., Foujols, M.-A., Gardoll, S., Gastineau, G., Ghattas, J., Grandpeix, J.-Y., Guenet, B., Guez, L. E., Guilyardi, E., Guimberteau, M., Hauglustaine, D., Hourdin, F., Idelkadi, A., Joussaume, S., Kageyama, M., Khodri, M., Krinner, G., Lebas, N., Levavasseur, G., Lévy, C., Li, L., Lott, F., Lurton, T., Luyssaert, S., Madec, G., Madeleine, J.-B., Maignan, F., Marchand, M., Marti, O., Mellul, L., Meurdesoif, Y., Mignot, J., Musat, I., Ottlé, C., Peylin, P., Planton, Y., Polcher, J., Rio, C., Rochetin, N., Rousset, C., Sepulchre, P., Sima, A., Swingedouw, D., Thiéblemont, R., Traore, A. K., Vancoppenolle, M., Vial, J., Vialard, J., Viovy, N., and Vuichard, N.: Presentation and evaluation of the IPSL-CM6A-LR climate model, J. Adv. Model. Earth Sy., 12, e2019MS002010, https://doi.org/10.1029/2019MS002010, 2020.

Carslaw, K. S., Lee, L. A., Reddington, C. L., Pringle, K. J., Rap, A., Forster, P. M., Mann, G. W., Spracklen, D. V., Woodhouse, M. T., Regayre, L. A., and Pierce, J. R.: Large contribution of natural aerosols to uncertainty in indirect forcing, Nature, 503, 67–71, https://doi.org/10.1038/nature12674, 2013.

Danabasoglu, G., Lamarque, J.-F., Bacmeister, J., Bailey, D. A., DuVivier, A. K., Edwards, J., Emmons, L. K., Fasullo, J., Garcia, R., Gettelman, A., Hannay, C., Holland, M. M., Large, W. G., Lauritzen, P. H., Lawrence, D. M., Lenaerts, J. T. M., Lindsay, K., Lipscomb, W. H., Mills, M. J., Neale, R., Oleson, K. W., Otto-Bliesner, B., Phillips, A. S., Sacks, W., Tilmes, S., van Kampenhout, L., Vertenstein, M., Bertini, A., Dennis, J., Deser, C., Fischer, C., Fox-Kemper, B., Kay, J. E., Kinnison, D., Kushner, P. J., Larson, V. E., Long, M. C., Mickelson, S., Moore, J. K., Nienhouse, E., Polvani, L., Rasch, P. J., and Strand, W. G.: The Community Earth System Model version 2 (CESM2), J. Adv. Model. Earth Sy., 12, e2019MS001916, https://doi.org/10.1029/2019MS001916, 2020.

https://doi.org/10.5194/egusphere-2026-6745
Preprint. Discussion started: 17 November 2026
© Author(s) 2026. CC BY 4.0 License.

Duan, K., Thompson, L. G., Yao, T., Davis, M. E., and Mosley-Thompson, E.: A 1000 year history of atmospheric sulfate concentrations in southern Asia as recorded by a Himalayan ice core, Geophys. Res. Lett., 34, L01810, https://doi.org/10.1029/2006GL027456, 2007.

E, C., Sun, Y., Li, Y., and Ma, X.: The atmospheric composition changes above the West Kunlun Mountain, Qinghai-Tibetan Plateau, in: Proceedings of the 2016 International Conference on Civil, Transportation and Environment, Atlantis Press, 961–968, https://doi.org/10.2991/iccte-16.2016.167, 2016.

Emmons, L. K., Schwantes, R. H., Orlando, J. J., Tyndall, G., Kinnison, D., Lamarque, J.-F., Marsh, D., Mills, M. J., Tilmes, S., Bardeen, C., Buchholz, R. R., Conley, A., Gettelman, A., Garcia, R., Simpson, I., Blake, D. R., Meinardi, S., and Pétron, G.: The chemistry mechanism in the Community Earth System Model version 2 (CESM2), J. Adv. Model. Earth Sy., 12, e2019MS001882, https://doi.org/10.1029/2019MS001882, 2020.

Eyring, V., Bony, S., Meehl, G. A., Senior, C. A., Stevens, B., Stouffer, R. J., and Taylor, K. E.: Overview of the Coupled Model Intercomparison Project Phase 6 (CMIP6) experimental design and organization, Geosci. Model Dev., 9, 1937–1958, https://doi.org/10.5194/gmd-9-1937-2016, 2016.

Gettelman, A., Mills, M. J., Kinnison, D. E., Garcia, R. R., Smith, A. K., Marsh, D. R., Tilmes, S., Vitt, F., Bardeen, C. G., McInerny, J., Liu, H.-L., Solomon, S. C., Polvani, L. M., Emmons, L. K., Lamarque, J.-F., Richter, J. H., Glanville, A. S., Bacmeister, J. T., Phillips, A. S., Neale, R. B., Simpson, I. R., DuVivier, A. K., Hodzic, A., and Randel, W. J.: The Whole Atmosphere Community Climate Model version 6 (WACCM6), J. Geophys. Res.-Atmos., 124, 12380–12403, https://doi.org/10.1029/2019JD030943, 2019.

Grigholm, B., Mayewski, P. A., Kang, S., Zhang, Y., Kaspari, S., Sneed, S. B., and Zhang, Q.: Atmospheric soluble dust records from a Tibetan ice core: Possible climate proxies and teleconnection with the Pacific Decadal Oscillation, J. Geophys. Res.-Atmos., 114, D20118, https://doi.org/10.1029/2008JD011242, 2009.

Hajima, T., Watanabe, M., Yamamoto, A., Tatebe, H., Noguchi, M. A., Abe, M., Ohgaito, R., Ito, A., Yamazaki, D., Okajima, H., Ito, A., Takata, K., Ogochi, K., Watanabe, S., and Kawamiya, M.: Development of the MIROC-ES2L Earth system model and the evaluation of biogeochemical processes and feedbacks, Geosci. Model Dev., 13, 2197–2244, https://doi.org/10.5194/gmd-13-2197-2020, 2020.

Harris, I., Osborn, T. J., Jones, P., and Lister, D.: Version 4 of the CRU TS monthly high-resolution gridded multivariate climate dataset, Sci. Data, 7, 109, https://doi.org/10.1038/s41597-020-0453-3, 2020.

Hersbach, H., Bell, B., Berrisford, P., Hirahara, S., Horányi, A., Muñoz-Sabater, J., Nicolas, J., Peubey, C., Radu, R., Schepers, D., Simmons, A., Soci, C., Abdalla, S., Abellan, X., Balsamo, G., Bechtold, P., Biavati, G., Bidlot, J., Bonavita, M., De Chiara, G., Dahlgren, P., Dee, D., Diamantakis, M., Dragani, R., Flemming, J., Forbes, R., Fuentes, M., Geer, A., Haimberger, L., Healy, S., Hogan, R. J., Hólm, E., Janisková, M., Keeley, S., Laloyaux, P., Lopez, P., Lupu, C., Radnoti, G., de Rosnay, P., Rozum, I., Vamborg, F., Villaume, S., and Thépaut, J.-N.: The ERA5 global reanalysis, Q. J. Roy. Meteor. Soc., 146, 1999–2049, https://doi.org/10.1002/qj.3803, 2020.

Hoesly, R. M., Smith, S. J., Feng, L., Klimont, Z., Janssens-Maenhout, G., Pitkanen, T., Seibert, J. J., Vu, L., Andres, R. J., Bolt, R. M., Bond, T. C., Dawidowski, L., Kholod, N., Kurokawa, J.-I., Li, M., Liu, L., Lu, Z.,

https://doi.org/10.5194/egusphere-2026-6745
Preprint. Discussion started: 17 November 2026
© Author(s) 2026. CC BY 4.0 License.

Moura, M. C. P., O'Rourke, P. R., and Zhang, Q.: Historical (1750–2014) anthropogenic emissions of reactive gases and aerosols from the Community Emissions Data System (CEDS), Geosci. Model Dev., 11, 369–408, https://doi.org/10.5194/gmd-11-369-2018, 2018.

Iizuka, Y., Uemura, R., Matsui, H., Oshima, N., Kawakami, K., Hattori, S., Ohno, H., and Matoba, S.: High flux of small sulfate aerosols during the 1970s reconstructed from the SE-Dome ice core in Greenland, J. Geophys. Res.-Atmos., 127, e2022JD036880, https://doi.org/10.1029/2022JD036880, 2022.

Jongebloed, U. A., Schauer, A. J., Hattori, S., Cole-Dai, J., Larrick, C. G., Salimi, S., Edouard, S. R., Geng, L., and Alexander, B.: Sulfur isotopes quantify the impact of anthropogenic activities on industrial-era Arctic sulfate in a Greenland ice core, Environ. Res. Lett., 18, 074020, https://doi.org/10.1088/1748-9326/acdc3d, 2023.

Kelley, M., Schmidt, G. A., Nazarenko, L. S., Bauer, S. E., Ruedy, R., Russell, G. L., Ackerman, A. S., Aleinov, I., Bauer, M., Bleck, R., Canuto, V., Cesana, G., Cheng, Y., Clune, T. L., Cook, B. I., Cruz, C. A., Del Genio, A. D., Elsaesser, G. S., Faluvegi, G., Kiang, N. Y., Kim, D., Lacis, A. A., Leboissetier, A., LeGrande, A. N., Lo, K. K., Marshall, J., Matthews, E. E., McDermid, S., Mezuman, K., Miller, R. L., Murray, L. T., Oinas, V., Orbe, C., Pérez García-Pando, C., Perlwitz, J. P., Puma, M. J., Rind, D., Romanou, A., Shindell, D. T., Sun, S., Tausnev, N., Tsigaridis, K., Tselioudis, G., Weng, E., Wu, J., and Yao, M.-S.: GISS-E2.1: Configurations and climatology, J. Adv. Model. Earth Sy., 12, e2019MS002025, https://doi.org/10.1029/2019MS002025, 2020.

Li, X., Ding, Y., Yu, Z., Sillanpää, M., Liu, S., Shangguan, D., and Lu, C.: An 80-year summer temperature history from the Xiao Dongkemadi ice core in the central Tibetan Plateau and its association with atmospheric circulation, J. Asian Earth Sci., 98, 285–295, https://doi.org/10.1016/j.jseaes.2014.09.025, 2015.

Liu, X., Xu, B., Yao, T., Wang, N., and Wu, G.: Carbonaceous particles in Muztagh Ata ice core, West Kunlun Mountains, China, Chinese Sci. Bull., 53, 3379–3386, https://doi.org/10.1007/s11434-008-0294-5, 2008.

MacFerrin, M., Amante, C., Carignan, K., Love, M., and Lim, E.: The Earth Topography 2022 (ETOPO 2022) global DEM dataset, Earth Syst. Sci. Data, 17, 1835–1849, https://doi.org/10.5194/essd-17-1835-2025, 2025.

Mauritsen, T., Bader, J., Becker, T., Behrens, J., Bittner, M., Brokopf, R., Brovkin, V., Claussen, M., Crueger, T., Esch, M., Fast, I., Fiedler, S., Fläschner, D., Gayler, V., Giorgetta, M., Goll, D. S., Haak, H., Hagemann, S., Hedemann, C., Hohenegger, C., Ilyina, T., Jahns, T., Jimenéz-de-la-Cuesta, D., Jungclaus, J., Kleinen, T., Kloster, S., Kracher, D., Kinne, S., Kleberg, D., Lasslop, G., Kornblueh, L., Marotzke, J., Matei, D., Meraner, K., Mikolajewicz, U., Modali, K., Möbis, B., Müller, W. A., Nabel, J. E. M. S., Nam, C. C. W., Notz, D., Nyawira, S.-S., Paulsen, H., Peters, K., Pincus, R., Pohlmann, H., Pongratz, J., Popp, M., Raddatz, T. J., Rast, S., Redler, R., Reick, C. H., Rohrschneider, T., Schemann, V., Schmidt, H., Schnur, R., Schulzweida, U., Six, K. D., Stein, L., Stemmler, I., Stevens, B., von Storch, J.-S., Tian, F., Voigt, A., de Vrese, P., Wieners, K.-H., Wilkenskjeld, S., Winkler, A., and Roeckner, E.: Developments in the MPI-M Earth System Model version 1.2 (MPI-ESM1.2) and its response to increasing $CO_2$, J. Adv. Model. Earth Sy., 11, 998–1038, https://doi.org/10.1029/2018MS001400, 2019.

Moseid, K. O., Schulz, M., Eichler, A., Schwikowski, M., McConnell, J. R., Olivié, D., Criscitiello, A. S., Kreutz,

https://doi.org/10.5194/egusphere-2026-6745
Preprint. Discussion started: 17 November 2026
© Author(s) 2026. CC BY 4.0 License.

K. J., and Legrand, M.: Using ice cores to evaluate CMIP6 aerosol concentrations over the historical era, J. Geophys. Res.-Atmos., 127, e2021JD036105, https://doi.org/10.1029/2021JD036105, 2022.

Qin, D., Hou, S., Zhang, D., Ren, J., Kang, S., Mayewski, P. A., and Wake, C. P.: Preliminary results from the chemical records of an 80.4 m ice core recovered from East Rongbuk Glacier, Qomolangma (Mount Everest), Himalaya, Ann. Glaciol., 35, 278–284, https://doi.org/10.3189/172756402781816799, 2002.

Sellar, A. A., Jones, C. G., Mulcahy, J. P., Tang, Y., Yool, A., Wiltshire, A., O'Connor, F. M., Stringer, M., Hill, R., Palmieri, J., Woodward, S., de Mora, L., Kuhlbrodt, T., Rumbold, S. T., Kelley, D. I., Ellis, R., Johnson, C. E., Walton, J., Abraham, N. L., Andrews, M. B., Andrews, T., Archibald, A. T., Berthou, S., Burke, E., Blockley, E., Carslaw, K., Dalvi, M., Edwards, J., Folberth, G. A., Gedney, N., Griffiths, P. T., Harper, A. B., Hendry, M. A., Hewitt, A. J., Johnson, B., Jones, A., Jones, C. D., Keeble, J., Liddicoat, S., Morgenstern, O., Parker, R. J., Predoi, V., Robertson, E., Siahaan, A., Smith, R. S., Swaminathan, R., Woodhouse, M. T., Zeng, G., and Zerroukat, M.: UKESM1: Description and evaluation of the U.K. Earth System Model, J. Adv. Model. Earth Sy., 11, 4513–4558, https://doi.org/10.1029/2019MS001739, 2019.

Sepulchre, P., Caubel, A., Ladant, J.-B., Bopp, L., Boucher, O., Braconnot, P., Brockmann, P., Cozic, A., Donnadieu, Y., Dufresne, J.-L., Estella-Perez, V., Ethé, C., Fluteau, F., Foujols, M.-A., Gastineau, G., Ghattas, J., Hauglustaine, D., Hourdin, F., Kageyama, M., Khodri, M., Marti, O., Meurdesoif, Y., Mignot, J., Sarr, A.-C., Servonnat, J., Swingedouw, D., Szopa, S., and Tardif, D.: IPSL-CM5A2 – an Earth system model designed for multi-millennial climate simulations, Geosci. Model Dev., 13, 3011–3053, https://doi.org/10.5194/gmd-13-3011-2020, 2020.

Tatebe, H., Ogura, T., Nitta, T., Komuro, Y., Ogochi, K., Takemura, T., Sudo, K., Sekiguchi, M., Abe, M., Saito, F., Chikira, M., Watanabe, S., Mori, M., Hirota, N., Kawatani, Y., Mochizuki, T., Yoshimura, K., Takata, K., O'ishi, R., Yamazaki, D., Suzuki, T., Kurogi, M., Kataoka, T., Watanabe, M., and Kimoto, M.: Description and basic evaluation of simulated mean state, internal variability, and climate sensitivity in MIROC6, Geosci. Model Dev., 12, 2727–2765, https://doi.org/10.5194/gmd-12-2727-2019, 2019.

Tegen, I., Neubauer, D., Ferrachat, S., Siegenthaler-Le Drian, C., Bey, I., Schutgens, N., Stier, P., Watson-Parris, D., Stanelle, T., Schmidt, H., Rast, S., Kokkola, H., Schultz, M., Schroeder, S., Daskalakis, N., Barthel, S., Heinold, B., and Lohmann, U.: The global aerosol–climate model ECHAM6.3–HAM2.3 – Part 1: Aerosol evaluation, Geosci. Model Dev., 12, 1643–1677, https://doi.org/10.5194/gmd-12-1643-2019, 2019.

Thompson, L. G., Mosley-Thompson, E., Davis, M. E., Bolzan, J. F., Dai, J., Klein, L., Gundestrup, N., Yao, T., Wu, X., and Xie, Z.: Glacial stage ice-core records from the subtropical Dunde ice cap, China, Ann. Glaciol., 14, 288–297, https://doi.org/10.3189/S0260305500008776, 1990.

Thompson, L. G., Yao, T., Davis, M. E., Mosley-Thompson, E., Wu, G., Porter, S. E., Xu, B., Lin, P.-N., Wang, N., Beaudon, E., Duan, K., Sierra-Hernández, M. R., and Kenny, D. V.: Ice core records of climate variability on the Third Pole with emphasis on the Guliya ice cap, western Kunlun Mountains, Quaternary Sci. Rev., 188, 1–14, https://doi.org/10.1016/j.quascirev.2018.03.003, 2018.

https://doi.org/10.5194/egusphere-2026-6745
Preprint. Discussion started: 17 November 2026
© Author(s) 2026. CC BY 4.0 License.

Thompson, L. G., Yao, T., Mosley-Thompson, E., Davis, M. E., Henderson, K. A., and Lin, P.-N.: A high-resolution millennial record of the South Asian monsoon from Himalayan ice cores, Science, 289, 1916–1919, https://doi.org/10.1126/science.289.5486.1916, 2000.

Turnock, S. T., Allen, R. J., Andrews, M., Bauer, S. E., Deushi, M., Emmons, L., Good, P., Horowitz, L., John, J. G., Michou, M., Nabat, P., Naik, V., Neubauer, D., O'Connor, F. M., Olivié, D., Oshima, N., Schulz, M., Sellar, A., Shim, S., Takemura, T., Tilmes, S., Tsigaridis, K., Wu, T., and Zhang, J.: Historical and future changes in air pollutants from CMIP6 models, Atmos. Chem. Phys., 20, 14547–14579, https://doi.org/10.5194/acp-20-14547-2020, 2020.

Twomey, S.: The influence of pollution on the shortwave albedo of clouds, J. Atmos. Sci., 34, 1149–1152, https://doi.org/10.1175/1520-0469(1977)034<1149:TIOPOT>2.0.CO;2, 1977.

van Marle, M. J. E., Kloster, S., Magi, B. I., Marlon, J. R., Daniau, A.-L., Field, R. D., Arneth, A., Forrest, M., Hantson, S., Kehrwald, N. M., Knorr, W., Lasslop, G., Li, F., Mangeon, S., Yue, C., Kaiser, J. W., and van der Werf, G. R.: Historic global biomass burning emissions for CMIP6 (BB4CMIP) based on merging satellite observations with proxies and fire models (1750–2015), Geosci. Model Dev., 10, 3329–3357, https://doi.org/10.5194/gmd-10-3329-2017, 2017.

Wang, C., Tian, L., Shao, L., and Li, Y.: Glaciochemical records for the past century from the Qiangtang Glacier No. 1 ice core on the central Tibetan Plateau: Likely proxies for climate and atmospheric circulations, Atmos. Environ., 197, 66–76, https://doi.org/10.1016/j.atmosenv.2018.10.028, 2019.

Yang, D., Yao, T., Wu, G., Zhao, H., Zhu, M., Deji, Qu, D., and Shi, Y.: Identifying the natural and agricultural impacts on the glaciochemistry of the Aru ice core on the northwestern Tibetan Plateau, Sci. Total Environ., 906, 167501, https://doi.org/10.1016/j.scitotenv.2023.167501, 2024.

Yang, D., Yao, T., Wu, G., Zhu, M., Zhao, H., Deji, Shi, Y., and Qu, D.: Different patterns and origins between northwestern and southeastern Tibetan ice core glaciochemical records over the past century, Sci. Total Environ., 819, 153195, https://doi.org/10.1016/j.scitotenv.2022.153195, 2022.

Yukimoto, S., Kawai, H., Koshiro, T., Oshima, N., Yoshida, K., Urakawa, S., Tsujino, H., Deushi, M., Tanaka, T., Hosaka, M., Yabu, S., Yoshimura, H., Shindo, E., Mizuta, R., Obata, A., Adachi, Y., and Ishii, M.: The Meteorological Research Institute Earth System Model version 2.0, MRI-ESM2.0: Description and basic evaluation of the physical component, J. Meteorol. Soc. Jpn. Ser. II, 97, 931–965, https://doi.org/10.2151/jmsj.2019-051, 2019.

Zhang, Y., Kang, S., Grigholm, B., Zhang, Y., Kaspari, S., Morgenstern, U., Ren, J., Qin, D., Mayewski, P. A., Zhang, Q., Cong, Z., Sillanpää, M., Schwikowski, M., and Chen, F.: Twentieth-century warming preserved in a Geladaindong mountain ice core, central Tibetan Plateau, Ann. Glaciol., 57, 70–80, https://doi.org/10.3189/2016AoG71A001, 2016.

Zhao, H., Xu, B., Yao, T., Tian, L., and Li, Z.: Records of sulfate and nitrate in an ice core from Mount Muztagata, central Asia, J. Geophys. Res.-Atmos., 116, D13304, https://doi.org/10.1029/2011JD015735, 2011.

https://doi.org/10.5194/egusphere-2026-6745
Preprint. Discussion started: 17 November 2026
© Author(s) 2026. CC BY 4.0 License.

574 Zhu, J., Xia, X., Che, H., Wang, J., Cong, Z., Zhao, T., Kang, S., Zhang, X., Yu, X., and Zhang, Y.:
575 Spatiotemporal variation of aerosol and potential long-range transport impact over the Tibetan Plateau, China,
576 Atmos. Chem. Phys., 19, 14637–14656, https://doi.org/10.5194/acp-19-14637-2019, 2019.

577 Zou, X., Hou, S., Zhang, W., Liu, K., Yu, J., Pang, H., and Liu, Y.: An increase of ammonia emissions from
578 terrestrial ecosystems on the Tibetan Plateau since 1980 deduced from ice core record, Environ. Pollut., 262,
579 114314, https://doi.org/10.1016/j.envpol.2020.114314, 2020.